Simulations and analytic models of ion guiding through a nanocapillary in insulating polymers

N. Stolterfoht
Helmholtz-Zentrum Berlin für Materialien und Energie, D-14109 Berlin, Germany
(Received 21 January 2013; revised manuscript received 14 February 2013; published 25 March 2013)

Simulations of ion guiding through an insulating cylindrical nanocapillary are performed in continuation of a recent theoretical work [N. Stolterfoht, Phys. Rev. A **87**, 012902 (2013)]. The ions are assumed to move on classical trajectories affected by the electric field primarily produced by the charge patch deposited near the capillary entrance. The deposited charges are transported along the capillary wall using a nonlinear conductivity law. Calculations for different capillary tilt angles from 0° to 8° are performed and compared with previous experimental results. The main focus of the analysis is to reveal unknown guiding mechanisms by a detailed investigation of the calculated results. Surprisingly, after reaching a maximum, the field component perpendicular to the capillary axis is found to decrease with increasing charge inserted into the capillary. At equilibrium, this field is nearly constant in all directions of the capillary along the entrance charge patch. The extension of this charge patch increases with increasing tilt angle although a simple picture of undeflected ions predicts the opposite behavior. These unexpected results simplify the theoretical treatment so that analytical expressions could be derived describing essential properties of the ion guiding. In particular, unknown parameters previously introduced in semiempirical models are interpreted.

DOI: 10.1103/PhysRevA.87.032901 PACS number(s): 61.85.+p, 34.50.Fa, 32.80.Fb

I. INTRODUCTION

In the past few years, considerable effort has been devoted to studies of ion guiding through capillaries in highly insulating materials. Ions entering into a capillary may hit the surface, leaving their charge at the inner capillary wall. When the capillary axis is tilted with respect to the incident beam direction, a charge patch is produced in the entrance region of the capillary, where a repulsive electric field is created. After sufficient charge deposition this field deflects the following ions in the direction of the capillary exit. Hence, the ions are guided through the capillary. The deflection at the charge patch occurs at relatively large distances from the capillary wall so that the incident charge state of the ions is maintained during their passage through the capillary. The outstanding property of the ion guiding is a self-organizing process [1], which determines the balance between charge deposition, charge transport, and ion deflection inside the capillaries.

The initial studies of the ion-guiding phenomenon in insulating materials have been performed using capillaries in polyethylene terephthalate (PET) [1–3]. During recent years the interest in this field has increased and researchers in several laboratories performed experimental studies with PET [4–10], polycarbonate (PC) [11,12], SiO_2 [13], and Al_2O_3 [14–16]. Specific studies devoted to the dynamic aspects of capillary guiding involving temporary charge patches have recently been conducted [17–20], where oscillatory variations of the ion emission angle have been observed. Also, electrons and ions have been used as projectiles guided through multitudes of nanocapillaries, single capillaries, and parallel glass plates. A more complete set of references to the earlier work can be found in reports of recent capillary studies [21,22].

In experimental works [2,3] it was empirically found that the equilibrium fraction of the transmitted ions is well described by a Gaussian function for which the fraction of transmitted ions decreases exponentially with the square of the tilt angle ψ. The ability of insulating capillaries to guide ions, referred to as the guiding power, can be characterized by the *guiding angle* ψ_c, for which the normalized transmission fraction drops to $1/e$. It was shown that the guiding angle can well be scaled by the charge-to-energy ratio of the incident ion [7,12]. However, the guiding angle also depends on an unknown parameter with the dimension of a potential, whose interpretation needs further consideration.

A series of pioneering theoretical studies [23–27] have provided detailed information about the guiding mechanisms. Those studies were based on simulations using a diffusion model, which treats the transport of the deposited charges as a random walk along the capillary surface. Similar simulations were performed in a recent work by the author [28], referred to as (I) in the following. In (I) a different concept is used involving a nonlinear charge transport model based on the formalism by Frenkel [29]. This model is supported by experiments [6], wherein it was shown that the transmitted ion fraction is nearly constant with respect to a change of the incident ion current by two orders of magnitude.

In the present work, simulations of ion guiding through an insulating capillary are performed using the theoretical methods described in (I). The previous calculations are extended for different tilt angles within the range from 0° to 8°. The simulations reveal surprising features of the guiding phenomenon. For instance, the field component perpendicular to the capillary axis, responsible for the ion deflection, is nearly constant over the length of the entrance patch and the distance perpendicular to the patch. It even remains constant when the capillary tilt angle changes. Moreover, the extension of the charge patch along the capillary axis does not decrease but increases with tilt angle. These unexpected results simplify the quantitative treatment, allowing for the derivatation of analytical expressions for the capillary guiding. Also, the analytical formalism provides plausibility for the common use of a Gaussian function fitting the fraction of transmitted ions and clarifies the origin of the unknown potential governing the guiding angle.

II. PREVIOUS EXPERIMENTS AND MODELS

In this section a few experimental results for varying tilt angles are shown from previous work to provide the scope for the present simulations. Furthermore, the semiempirical Gaussian formula is presented that is frequently used in the literature. This formula will later be discussed on the basis of the analytical expressions derived from the results of the simulations.

Figure 1 shows typical examples for 3 keV Ne^{7+} ions transmitted through nanocapillaries in PC polymers [30]. To study dynamical guiding properties, the mean angle of the ions ejected from the capillary exit has been measured. The characteristic quantity, used to plot the experimental results, is the charge $Q_{in} = J_{in}t$ inserted into a single capillary. The inserted beam $J_{in} = J_d\,(d/D)^2$ can be obtained from the total ion beam J_d, where d and D are the diameters of the capillary and the incident beam, respectively. Since the inserted charge is proportional to the time t one can also speak of the time evolution of the measured quantities.

Figure 1 shows results for the tilt angles of $\psi = 3^\circ$, 5°, and 7°. For 3° and 5° the mean emission angles exhibit oscillations within about $\pm 1^\circ$ around a center angle equal to the tilt angle. These oscillations are expected to be produced by temporary charge patches formed in addition to the dominant charge patch at the capillary entrance [17,19,24]. Surprisingly, for the tilt angle of 7° no oscillations are observed, i.e., the mean angle remains constant with increasing charge insertion. Obviously, this last observation is a challenge for the simulations to reproduce the experimental data.

Apart from the mean emission angle, the experimental studies yield the fraction $f_t = J_t/J_{in}$ of transmitted ions, where J_t is the transmitted ion intensity. In general, this fraction increases with charge insertion from zero to a maximum at which the equilibrium of the ion guiding is reached [30]. For equilibrium, the tilt-angle dependence of the transmitted ion fraction can be fitted by a Gaussian-like function [5,31]

$$f_t = f_0 \exp\left(-\frac{\sin^2\psi}{\sin^2\psi_c}\right), \tag{1}$$

which allows for the determination of the guiding angle ψ_c by the fit procedure. The parameter $f_0 \lesssim 1$ is the transmitted ion fraction for $\psi = 0$, which accounts for the loss of ions due to the divergence of the incident beam.

It should be emphasized that Eq. (1) has frequently been used in the literature. Detailed studies of scaling rules have provided a semiempirical expression for the guiding angle [7,12],

$$\sin\psi_c = \left(\frac{qV_c}{T_p}\right)^{0.7}, \tag{2}$$

where q and T_p are the charge state and energy of the incident ion, respectively. The parameter V_c was introduced as an effective potential near the entrance patch, which was treated as an unknown quantity determined by the fit procedure. Altogether, formula (1) was derived by means of semiempirical methods, while an *ab initio* justification is still missing.

In particular, it is not clear that V_c can be assumed to be constant. For the sufficient deflection of an ion, the potential V_c must somehow balance the perpendicular ion energy T_y, which increases with $\sin^2\psi$. The ion deflection angle depends on the perpendicular field component as well as on the length of the entrance patch [30]. However, for unperturbed trajectories, the patch length z_ψ involves a decreasing dependence on the tilt angle:

$$z_\psi = \frac{d}{\sin\psi}, \tag{3}$$

where d is the capillary diameter. With these dependencies, intriguing questions arise about the interpretation of the potential V_c and, specifically, why it can be assumed to be independent of the tilt angle ψ. We shall return to these questions after deriving the analytical formalism.

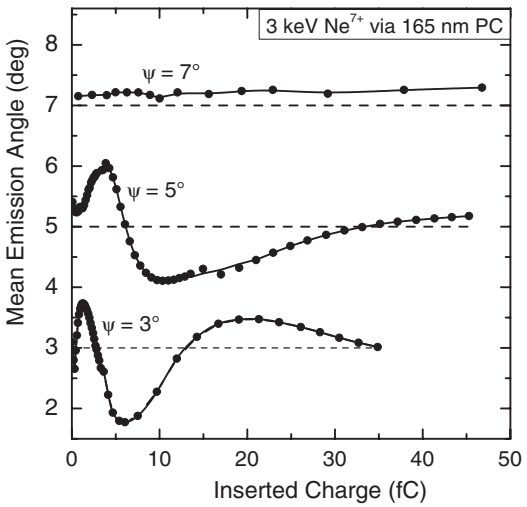

FIG. 1. Mean emission angle of the transmitted 3-keV Ne^{7+} ions for capillary tilt angles of 3°, 5°, and 7°. The capillaries in PC have a diameter of 165 nm and a length of 10 μm. Data taken from Ref. [30].

III. THEORETICAL METHOD

The concepts of the simulations are introduced in (I) so just a brief description is given here. The ions are inserted into the circular capillary under the tilt angle ψ using random distributions for the initial x and y values, where x and y are, respectively, the horizontal and vertical coordinates perpendicular to the capillary z axis. The incident ions that hit the inner capillary wall are assumed to deposit their full charge onto the surface. The parameters of the incident ions and the capillaries are summarized in Table I.

The surface charges produce an electric potential that was evaluated by accumulating the individual Coulomb potentials of the point charges. Trajectories of the ions were evaluated solving Newton's equation of motion for a classical particle moving in an electric field deduced from the potential. This part essentially represents an *ab initio* calculation as it includes no free parameter. The elaborate part of the calculation is the inclusion of the migration of the deposited charges. For the charge flow, which reduces the charge patches, it was assumed that the surface conductivity played the major role within the capillary.

TABLE I. Parameters used for the simulations. The energy and total current of the Ne^{7+} projectile are given together with the diameter, length, and tilt angles of the capillary.

Parameter	Value
Energy	3 keV
Current	100 pA
Diameter	200 nm
Length	10 μm
Tilt angles	3°, 5°, 7°

To evaluate the transport of the deposited charges we use the expression given by Frenkel [29], which describes the conductivity produced by thermal electron liberation from deep traps enhanced by the lowering of the potential barrier with a high electric field. In accordance with Frenkel's model, one may express the transition rate of a trapped electron into the continuum as a function of the electric field $E = |\mathbf{E}|$ as

$$\Gamma_s = \Gamma_0 \exp\left(\sqrt{\frac{E}{E_c}}\right) \quad \text{with} \quad E_c = \frac{\varepsilon(kT)^2}{e^3}, \tag{4}$$

where Γ_0 is the transition rate for $E \to 0$. The parameter E_c is a characteristic field governing the exponential increase of the surface current.

In the simulations we consider the deposition of positively charged ions creating a cluster of holes, which are readily captured at localized surface centers (traps). Unlike a liberated electron, which can freely move within the conduction band, a hole migrates in an insulator by performing a series of individual jumps (hops) from one trap to the next one [32,33]. Each transition requires the liberation of an electron into the conduction band, which fills the trap containing the hole. The hopping time τ of the hole is equal to the transfer time of the corresponding electron. Thus, this hopping time is obtained as $\tau = 1/\Gamma_s$ with Γ_s from Eq. (4).

As shown in detail in (I), within a macroscopic time Δt one obtains the directed hole transport length as

$$\Delta\mathbf{s} = \Delta t\, \mu_0 \mathbf{E} \exp\left(\sqrt{\frac{E}{E_c}}\right), \tag{5}$$

where μ_0 is the mobility of the charge carrier. The formula implies two regions where for $E \ll E_c$ the current follows a linear field dependence (as in Ohm's law) and for $E \gtrsim E_c$ the current is determined by an exponential (nonlinear) dependence. As in (I) the mobility was set as $\mu_0 = 0.01$ $\text{nm}^2/\text{V s}$ indicated in Table II. It should be added that the mobility μ_0 is proportional to the surface conductivity σ_0 for $E \to 0$. Hence changing the parameter μ_0 is in practice equivalent to changing the conductivity σ_0. Therefore, in the following the variation of μ_0 will also be referred to as a change of the surface conductivity.

TABLE II. Parameters used to evaluate the nonlinear transport of the charges on the capillary surface (see text).

Parameter	Value
E_c	1.33×10^{-3} V/nm
μ_0	0.01 $\text{nm}^2/\text{V s}$
Δt	5.6 s
τ_b	40 min

From the definition in Eq. (4) one obtains $E_c = 1.33 \times 10^{-3}$ V/nm at room temperature (Table II). The simulations show that a typical field within the capillary entrance region is of the order of 0.05 V/nm so that in general $E \gg E_c$, which implies that the exponential (nonlinear) term is dominant in Eq. (5).

The ion insertion and the charge flow were treated sequentially in iterations. After a small number of ions (typically $n_0 = 20$ out of several thousands) were inserted into the capillary, the deposited charges were displaced in proportion to the ion insertion time Δt. This time was determined from the incident ion current by

$$\Delta t = \frac{q n_0}{J_{in}}, \tag{6}$$

where q is the charge of the projectile. With the parameters used here it follows that $\Delta t = 5.6$ s.

With Eq. (5) the distance and direction of the charge displacement were determined with the electric field vector evaluated at the location of the charge under consideration. Thus, the charges were moved along the capillary wall parallel (longitudinal) and perpendicular (transverse) to the capillary z axis. When a charge reaches the entrance or exit of the capillary, it is depleted as it is assumed to disappear within the metal layers at the sample surfaces. Remarkably, as shown later, the charge patches are weakened more by the transverse charge flow at the capillary surface in the x-y direction than by the longitudinal flow in the z direction.

In contrast to the surface conductivity, the bulk conductivity was modeled as a diffusion of the deposited charge into the capillary material where it may be lost after a certain time [23,24]. In accordance with case (ii) in (I) the charges inside the bulk are treated with the same mobility as at the surface. This treatment implies a depletion of the charges following an exponential decay with the time constant $\tau_b = 40$ min (Table II) as in (I). Then, the charge depletion probability during the time interval Δt from Eq. (6) is obtained as $p_b = \Delta t/\tau_b$.

IV. RESULTS OF THE SIMULATIONS

A. Trajectories and charge distributions

The following simulations are devoted to the analysis of the ion guiding for various tilt angles. The calculations were performed with the parameters given in Tables I and II. In Fig. 2 trajectories and deposited charges are shown for the tilt angle of 3°. Figures 2(b)–2(f) indicate that a large number of ions are transmitted through the capillary. The ions follow oscillatory trajectories to the end of the capillary where they leave under varying angles. Finally, the ions are emitted parallel to the capillary axis in agreement with the experiments (Fig. 1). Similar results were calculated in (I) for the tilt angle of 5°, which will partially be shown for comparison in the following.

In the right-hand column of Fig. 2 the distributions of deposited charges are shown. In Fig. 2(a) the trajectories are all stopped inside the capillary. However, the deposited charge of $Q_{in} = 0.31$ fC produces a field component E_y that weakly deflects the ions so that they land at a location further inside

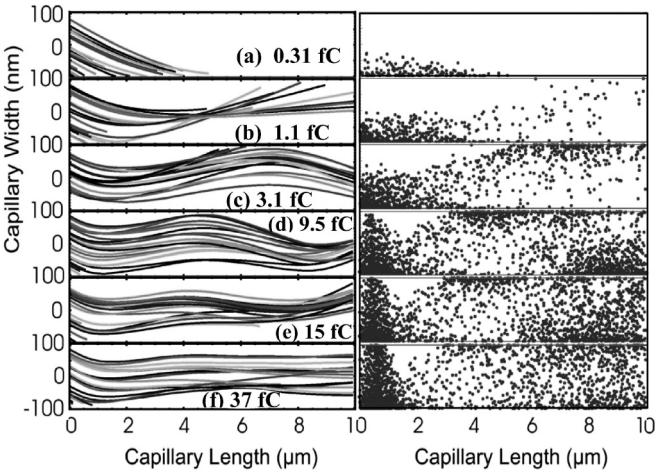

FIG. 2. Trajectories of 3-keV Ne^{7+} (left-hand panels) and corresponding distributions for the deposited charges (right-hand panels). The tilt angle is 3°. The inserted charge Q_{in} is indicated in each panel. The capillary length and width correspond to the capillary z and y axes, respectively.

the capillary. Thus, the length of the entrance charge patch is expanded. If the field E_y at the entrance patch becomes saturated due to the strong nonlinear charge removal, the patch is extended in length until it is able to deflect the ions towards the capillary exit [30].

In Fig. 2(b) the charge insertion is sufficiently high so that the ions are deflected to the upper wall near the capillary exit. One notes that the deflection of the ions inhibits the further deposition of the charges at larger distances inside the capillary. Thus, the entrance patch shrinks in comparison with the length predicted by Eq. (3), which is again part of the self-organizing property of the ion guiding. Also, one can observe a focusing of the ion trajectories, which is due to the increase of the field component E_y as y approaches the bottom of the capillary. However, from the other Figs. 2(c)–2(f) it is seen that the ion focusing diminishes as the charge deposition on the entrance charge patch increases. This can be explained by the migration of the charges to the opposite side of the capillary wall so that the field component E_y becomes essentially constant in the y direction.

In the right-hand column of Figs. 2(d) and 2(e) one can find two additional charge patches in the upper hemisphere near the center and at the lower hemisphere near the exit of the capillary. The additional patches change their position and strength as a result of the charge transport. Finally, at equilibrium these charge patches lose importance. In Fig. 2(f), where the ion guiding has achieved equilibrium, the charges are distributed all over the capillary wall. In particular, the entrance charge patch reveals the migration of the charges perpendicular to the capillary axis. A significant number of charges are visible in the upper half of the capillary, which cannot directly be reached by the incident ions. This migration to the opposite side of the capillary wall is an important effect, which governs the self-organizing behavior of the ion guiding.

In Fig. 3 the trajectories and charge distributions for the tilt angle 3° are compared with those for 0°, 5°, and 7°. For 0° the inserted charge is ∼20 fC. For the nonzero tilt angles the inserted charge amounts to ∼40 fC, which is sufficiently

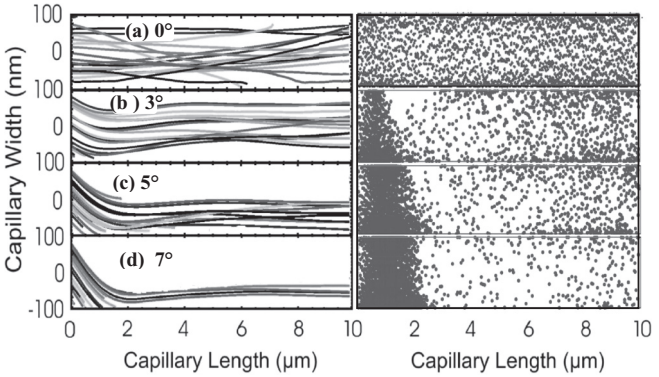

FIG. 3. Trajectories of 3-keV Ne^{7+} (left-hand panels) and corresponding distributions for the deposited charges (right-hand panels). In (a), (b), (c), and (d) the tilt angles are 0°, 3°, 5°, and 7°, respectively, as indicated in the panels. The inserted charge Q_{in} is equal to 20 fC for 0° and ∼40 fC for the other tilt angles.

high to reach equilibrium. The trajectories for the tilt angles 3°, 5°, and 7° are reflected at the entrance patch by an amount equal to the tilt angle so that they are directed to the capillary exit. At equilibrium the secondary charge patches play a minor role since they are essentially weakened by charge migration. Therefore the ions travel along nearly straight lines to the capillary exit (Fig. 3).

The distributions in the right-hand column of Fig. 3 show that the entrance patch contains an increasing amount of charge as the tilt angle increases. This is plausible since the ions entering with a larger angle need more field to be deflected. In fact, for ion deflection the transverse ion energy T_y must be reduced to zero by the repulsive field. Later in Sec. IV C, we shall see that, surprisingly, the deflection field barely increases with the tilt angle.

On the contrary, the extension of the field along the capillary axis rises with the tilt angle as can be seen from the charge distributions in the right-hand column of Fig. 3. The enhancement of the patch extension is highly unexpected, since the length of the charge patch produced by undeflected ions has the opposite tilt-angle dependence as indicated by Eq. (3). These opposite dependencies can be explained by the self-organizing property of the entrance charge patch, as will be discussed in more detail later.

B. Ion transmission and mean emission angle

To obtain more quantitative information from the simulations, the transmitted ion fraction f_t and the mean angle $\overline{\alpha} = n_t^{-1} \sum_i^{n_t} \alpha_i$ were evaluated, where α_i is the emission angle of the ith ion as in the experiments. Thus, a direct comparison is possible between the calculations and experimental data plotted in Fig. 1. Figure 4 shows the results of the simulations for both quantities f_t and $\overline{\alpha}$. The fraction f_t is zero for a short interval. From a certain threshold it rises to a sharp maximum and then tends to a constant value. The sharp maximum, which can be seen in Figs. 4(a)–4(c), has previously been identified as *overshoot* in experimental studies [19]. The constancy of the ion transmission is in accordance with the experimental data for PET reported in [30].

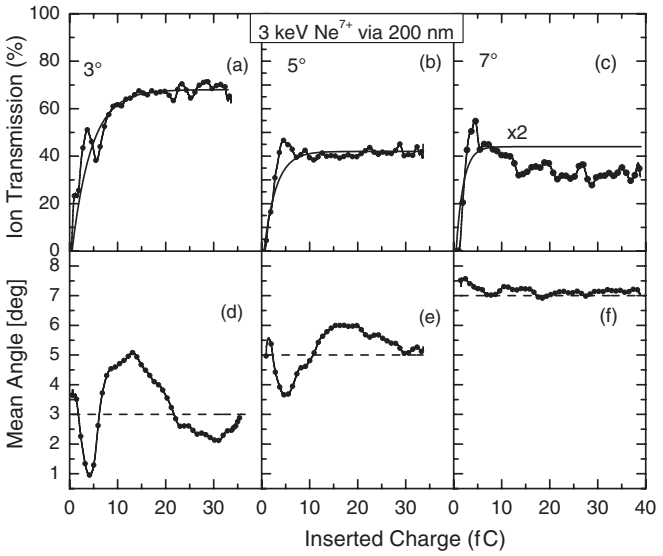

FIG. 4. Fraction of the ion transmission f_t and mean angle $\overline{\alpha}$ of the 3-keV Ne^{7+} ions ejected from the capillary exit. The data are obtained from simulations such as those given in Fig. 2. The three columns show results for the tilt angles of 3°, 5°, and 7°. The solid lines in the upper panels are fits to the data using an exponential charge-up function given in (I).

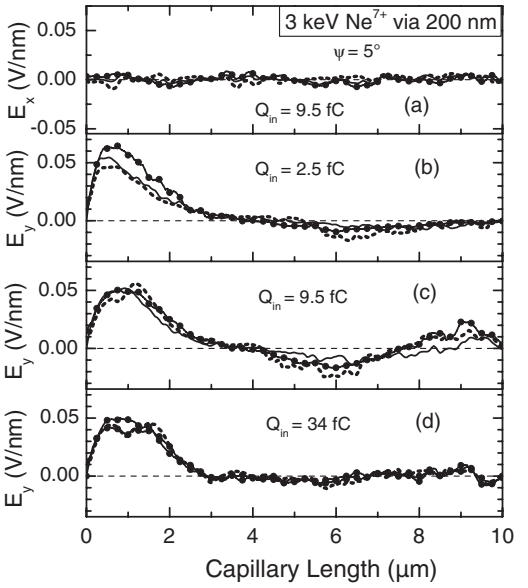

FIG. 5. Field components along the capillary z axis for the tilt angle of 5° calculated with the parameters from Tables I and II. In (a) the component E_x is shown for the charge insertion of 9.5 fC. In (b), (c), and (d) the component E_y is plotted for the charge insertions of $Q_{in} = 2.5$, 9.5, and 34 fC, respectively. The solid lines with points, the solid lines, and the dashed lines represent data for $y = -65, 0$, and 65 nm, respectively, where $x = 0$. The field E_x refers to $x = -65$, 0, and 65 nm with $y = 0$.

It should be noted that the calculations for the untilted capillary ($\psi = 0$) yielded an ion fraction of 85%, which is plausible in view of the beam divergence of $\pm 0.3°$. Figures 4(a)–4(c) show that the ion transmission at equilibrium decreases from 60% to 15% with increasing tilt angle. The tilt-angle dependence of the transmitted ion fraction is governed by the guiding angle, which will be discussed in Sec. V C.

In Figs. 4(d) and 4(e) the mean angle of the ions exhibits oscillations around the center angle (equal to the tilt angle). For 3° the oscillations can be verified from the trajectories in the left-hand column of Fig. 2. First, the ions are deflected from the entrance patch directly to the exit where they leave at angles as large as 4°, i. e., the sum of the center angle of 3° and the aspect angle of 1° [Fig. 2(b)]. Then the mean angle oscillates from values smaller than the center angle due to the deflection at the first transient charge patch [Fig. 2(c)] to values larger than the center angle due to the second transient charge patch [Fig. 2(c)]. These oscillations are in general agreement with the experimental results in Fig. 1. Figures 4(d) and 4(e) indicate that the frequency and the amplitude of the oscillations decrease with increasing tilt angle. The frequency behavior is also in agreement with the experiments (Fig. 1).

For the tilt angle of 7° the simulations confirm the missing oscillations of the mean emission angle observed experimentally in Fig. 1. This observation can be explained by a relatively fast migration of the deposited charges to the other side of the capillary wall, which inhibits the deflection of the incident ions by angles larger than the tilt angle. Thus, no secondary charge patches are produced, and oscillations of the mean emission angle are suppressed. This finding is also consistent with the fact that the transmitted ion fraction decreases with increasing charge insertion [Fig. 4(c)].

C. Potential and field components

To obtain more information about the ion-guiding mechanism, we consider the field components within the capillary evaluated for the tilt angle of 5°. Again, the calculations were performed using the parameters from Tables I and II. In Fig. 5 the results for the field components E_x and E_y are plotted along the z axis. In Fig. 5(a) the solid line with points, the solid line, and the dashed line represent the field component E_x at $y = 0$ for $x = -65, 0$, and 65 nm, respectively. Likewise, in Figs. 5(b)–5(d) the solid line with points, the solid line, and the dashed line represent E_y data at $x = 0$ for $y = -65$, 0, and 65 nm, respectively.

In Fig. 5(a) an example of the field component E_x is given for a charge insertion of 9.5 fC. This component is found to be rather small as it consists essentially of statistical noise. In fact, E_x turned out to be small at all locations within the capillary so that it will not be discussed any more in the following. Figures 5(b)–5(d) depicts the field component E_y for increasing charge insertion into the capillary, i.e., for 2.5, 9.5, and 34 fC. Within the entrance patch region these field components have a maximum reaching ~0.05 V/nm. Moreover, smaller E_y fields are present at the additional charge patches, seen primarily in Fig. 5(c).

In Fig. 5(b) the three curves at the entrance patch show that the field E_y increases somewhat with decreasing y. This finding is in agreement with the focusing effect already observed above in Fig. 2(b). As mentioned, the lowest trajectory is more deflected than the higher ones so that they cross within the capillary. However, the focusing effect was found to diminish with increasing charge insertion (Fig. 2). Indeed, from Figs. 5(c) and 5(d) it is seen that E_y is nearly

TABLE III. The maximum of the averaged field component E_y shown in Figs. 5(b)–5(d) for different values of the inserted charge Q_{in}. The tilt angle is 5° (see text).

Charge Q_{in} (fC)	Maximum E_y (V/nm)
2.5	0.055
9.5	0.051
34	0.042

TABLE IV. The maximum of the averaged field component E_y shown in Fig. 6(b) for different values of the tilt angle ψ. The inserted charge is equal to 34 fC (see text).

Angle ψ	Maximum E_y (V/nm)
3°	0.040
5°	0.042
7°	0.045

independent of y. A similar constancy was found for nearly all x and y coordinates, which greatly simplifies the further analysis of the ion deflection.

The major effect of the field component E_y is the deflection of the incident ions towards the capillary exit. Since E_y is nearly constant in the y direction, it is useful to consider the mean value $\overline{E}_y$ averaged over that coordinate. In the following, such mean values are used throughout, but they are still denoted E_y for simplicity. In Table III the column denoted "Maximum" contains mean values for E_y. Remarkably, Figs. 5(b)–5(d) suggest that E_y decreases with increasing charge insertion. Indeed, Table III confirms quantitatively that this field component decreases by 25% when the inserted charge rises from 2.5 to 34 fC.

Next, the results for additional tilt angles are considered. Figure 6 shows the potential V together with the field components E_y and E_z for $\psi = 3°$, 5°, and 7°. The data refer to a charge insertion of 34 fC, which is sufficiently large to achieve equilibrium. Near the entrance region, the potentials exhibit a maximum, which increases with tilt angle. Also, the maximum is shifted inside the capillary. Similar shifts are observed for the field components E_y and E_z. Obviously, the entrance charge patch is extended into the capillary interior when the tilt angle increases.

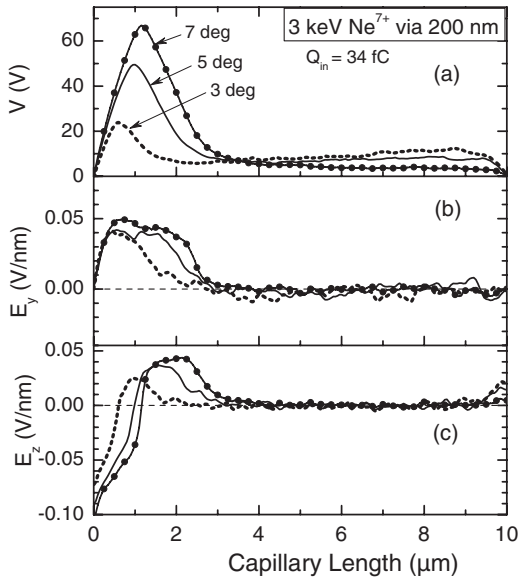

FIG. 6. Potential V and field components E_y and E_z. The data are calculated with the parameters shown in Tables I and II. The dashed line, solid line, and solid line with points represent data for the tilt angles of 3°, 5°, and 7°, respectively, where $x = y = 0$. The charge insertion is equal to 34 fC.

The maximum of the potential V is found to be as high as 70 V. This value is still significantly smaller than 420 V needed to create an potential barrier that cannot be overcome by the 3-keV Ne^{7+}ions as discussed in more detail in (I). Moreover, it is seen that the potential V rises rapidly, producing a field component E_z that reaches the value of 0.1 V/nm in Fig. 6(c). This field is close to the breakthrough value for polymers [34,35] so that the charges near the capillary entrance are rapidly transported to the grounded metal layer in front of the capillary.

The outstanding result of Fig. 6 is that the field component E_y remains nearly constant with varying tilt angle. It can be seen from the values in Table IV that E_y increases only by ∼10 % with tilt angle. Moreover, the curves in Fig. 6(b) indicate that the component E_y increases in the z direction with tilt angle. As already noted from Fig. 3, this length expansion is surprising, since the length produced by undeflected ions has the opposite tilt-angle dependence [Eq. (3)]. In the following, analytical models are presented, which confirm the unexpected expansion of the entrance charge patch.

V. ANALYTICAL DESCRIPTIONS

A. Deflection angle of the ion

In the foregoing sections the simulations provided detailed information about the field components near the entrance charge patch. The calculations revealed unexpected results. At equilibrium the deflecting field E_y is found to be rather constant with respect to the variation of the x and y coordinates. Also, this field is nearly constant within a certain z range covering the entrance patch. Furthermore, E_y barely changes when the tilt angle varies. These properties provide confidence that essential features of the ion guiding can be described by analytical models.

Let us first look at the ion deflection angle near the entrance patch. As a general case we consider the field component $E_y(\mathbf{r})$, which depends on all coordinates $\mathbf{r} = (x, y, z)$. As shown in detail previously [30], the ion deflection angle can be evaluated from the integration of the momenta obtained from the perpendicular field $E_y(\mathbf{r}(t))$. With the approximation $dt = dz/v$ one obtains

$$\sin\theta = \frac{q \int E_y(\mathbf{r}(z))dz}{2T_p} = \frac{qU_e}{2T_p}, \tag{7}$$

where q and T_p are again the projectile charge and energy, respectively. The quantity U_e is a path integral of the field

TABLE V. Results for parameters evaluated from the field component E_y shown in Figs. 5(b)–5(d), which provides information about the entrance charge patch for different values of the inserted charge Q_{in} (see text).

Charge Q_{in} (fC)	Integral U_e (V)	Length l_m (μm)	Deflection θ (deg)
2.5	93	1.7	6.2
9.5	91	1.8	6.1
34	82	1.9	5.5

component E_y along the trajectory of the incident ion,

$$U_e = \int E_y(\mathbf{r}(z))dz \tag{8}$$

It is realized that Eq. (7) is redundant, since with the knowledge of the ion trajectory, the deflection angle is already given. However, Eq. (7) is valuable when the field component E_y is constant with respect to the x and y coordinates as is the case in the present simulations. Then, $E_y(\mathbf{r}(z)) = E_y(z)$ depends only on the z coordinate and the path integral reduces to a simple integral over that coordinate.

To determine the quantity U_e, the field components E_y from Figs. 5(b)–5(d) were numerically integrated using Eq. (8) up to $z = 3$ nm. The results of the integration are given in the column denoted "Integral" of Table V, which has the dimension of a potential. Also in Table V the column denoted "Length" contains the effective length l_m of E_y derived from $l_m = U_e/E_y$. The length l_m is found to be nearly constant.

The integral U_e is a measure for the patch strength which determines the ion deflection angle θ [Eq. (7)]. In Table V the angle θ is shown in the last column labeled "Deflection." With the relatively small charge insertion of 2.5 fC this angle is 6.2°, which is larger than the sum of the tilt angle of 5° and the aspect angle of 1°, so that the ions hit the other side of the capillary, where they produce a secondary charge patch. At equilibrium the ions are deflected by 5.5°, which is a suitable angle to direct them from the capillary entrance straight to the exit. Hence, against our expectation, it should be kept in mind that the deflection angle decreases with increasing charge insertion.

Next, we consider the field components E_y in Fig. 6(b) for different tilt angles. Again, the results for U_e are determined by means of Eq. (8) and are given in Table VI. The integral U_e increases significantly with tilt angle although the field component E_y is nearly constant (Table IV). This is due to the extension of E_y along the z axis, which increases with tilt angle. The extension is confirmed by the increase of the effective length l_m given in Table VI. Again, it is noted that this result is unexpected since Eq. (3) implies the opposite tilt-angle dependence. This contradiction may be explained by the deflection of the ions that can change the size of the entrance patch during the charge deposition.

TABLE VI. Results for parameters evaluated from the field component E_y shown in Fig. 6(b), which provides information about the entrance charge patch for different values of the tilt angle ψ (see text).

Angle ψ (deg)	Integral U_e (V)	Length l_m (μm)	Deflection θ (deg)
3	54	1.3	3.6
5	82	1.8	5.5
7	105	2.3	7.1

Finally, the deflection angles were evaluated by means of Eq. (7). The results are given in the last columns of Table VI. In accordance with the rising U_e, the deflection angle θ increases significantly with tilt angle. In fact, the angle θ is found to be somewhat larger than the corresponding tilt angle that provides suitable conditions for the direct passage of the ions to the capillary exit. It is recalled that the data in Table IV refer to equilibrium conditions. In this case, a direct transmission occurs without additional charge patches, as can be seen from Fig. 3 for all tilt angles. Moreover, this observation confirms the experimental finding that at equilibrium the ions leave the capillary along the capillary axis.

B. Trajectories at the entrance patch

The following derivation of analytical expressions is based on the results of the simulations that the deflection field E_y changes only marginally with increasing tilt angle. On the other hand, the simulations indicate that E_y increases in length as the tilt angle increases. These counterintuitive observations will be verified by the analytical treatment of the ion trajectories shown in Fig. 7.

The constant field found here resembles the homogeneous field between charged parallel plates for which ion guiding has previously been studied [36]. Thus, for a circular capillary with a constant field component E_y and a minor component E_x, the ion trajectories follow a parabola which is given by the

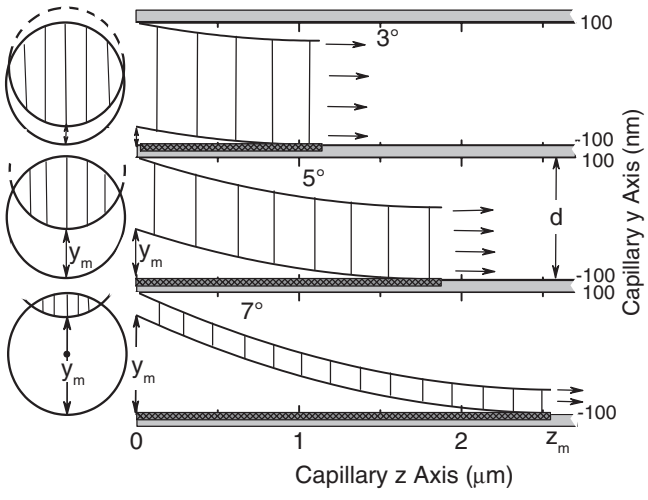

FIG. 7. Parabolic trajectories used to derive analytic expressions describing the ion transmission through capillaries. The graphs are associated with the tilt angles 3°, 5°, and 7°. The ions entering into the area, shaded by vertical lines, are assumed to be tranmitted to the capillary exit. The distancies z_m and y_m are given by Eqs. (10) and (11), respectively. Note that the length z_m of the entrance charge patch, represented by the horizontal black bar, is proportional to the tilt angle.

expression

$$y = y_0 + \frac{qE_y}{4T_p \cos^2 \psi}(z - z_m)^2, \tag{9}$$

where z_m is the distance from the capillary entrance to the parabola minimum. The decrease of the parabola between the entrance point y_0 and the minimum at z_m is denoted y_m as shown in Fig. 7.

The values z_m and y_m are obtained from the condition that the ions enter the capillary at the tilt angle ψ. Forming the derivative of y in Eq. (9), setting it equal to $\tan \psi$ at $z = 0$, and solving for z_m yields

$$z_m = \frac{2T_p}{qE_y} \cos \psi \sin \psi. \tag{10}$$

In general, for small tilt angles, one may set $\cos \psi \approx 1$. Likewise y_m may be obtained as

$$y_m = \frac{T_p}{qE_y} \sin^2 \psi. \tag{11}$$

It should be noted that the length z_m is proportional to $\sin \psi$ and the height y_m depends on its square, $\sin^2 \psi$.

To analyze the range of the possible ion transmission, two limiting trajectories are considered in Fig. 7. The higher one starts at the upper edge of the capillary wall and it follows a parabolic curve to its minimum. In Fig. 7 the drawing of each parabola stops at its minimum, where its derivative is equal to zero. The lower trajectory starts at y_m, follows again a parabolic curve, and reaches its minimum at the bottom of the capillary wall where the ion charge is supposed to be deposited.

All ions starting beyond the lower trajectory (i.e., within the range denoted y_m) hit the lower capillary wall where they enhance the entrance charge patch. The trajectories outside the y_m region cannot reach the lower capillary wall. Therefore, the farthest deposition inside the capillary is governed by the lower trajectory which hits the capillary wall at z_m. The length of the entrance patch is limited by z_m as indicated by the dark horizontal bars at the bottom of the capillary. In Table VII the length z_m is given as calculated by means of Eq. (10), which are in reasonable agreement with the corresponding length l_m in Table VI. In particular, the longitudinal size of the entrance patch increases linearly with $\sin \psi \approx \psi$. Thus, the present analytical description confirms the surprising results of the simulations that the patch length is proportional rather than inversely proportional to the tilt angle ψ.

All ions entering into the capillary between the two limiting trajectories (the region shaded by perpendicular lines) follow parabolic curves until their minimum is reached at z_m. Since the charge patch ends at this minimum, the ions are not further deflected so that they may propagate to the capillary exit on a near horizontal trajectory. From Fig. 7 it can be seen that the width of the shaded range, given by $d - y_m$, decreases significantly with the tilt angle. This finding is responsible for the decrease of the ion transmission with increasing tilt angle. A quantitative analysis of the transmitted ion fraction will be performed in the next section.

TABLE VII. Results for the parameters y_m and z_m evaluated by Eqs. (11) and (10), respectively, for different tilt angles ψ. The data are based on the E_y field also shown in Table IV (see text).

Angle ψ (deg)	Field E_y (V/nm)	Height y_m (nm)	Length z_m (μm)
3	0.040	29	1.12
5	0.042	82	1.87
7	0.045	162	2.63

C. Transmitted ion fraction

Looking back at Fig. 4, it is recalled that the simulation yielded the equilibrium fraction f_t of transmitted ions for various tilt angles. In Fig. 8 these results are summarized as thick points labeled "Simulations." The data were fitted by Eq. (1) introduced in Sec. II. The fit results are given by the dashed line, which compares very well with the data points. The fit yields the guiding angle of $\psi_c = 5.6^\circ$, which is in good agreement with the experimental result of 5.3° used to establish a scaling law for ion guiding [7,12].

In the following, the fraction of transmitted ions is evaluated in closed form on the basis of the scenario depicted in Fig. 7. For this purpose, the circular shape of the capillary is taken into account, assuming an ion beam of homogeneous density. In the foregoing section only ions were considered that are incident at the vertical center axis for which $x = 0$. To generalize this treatment, we consider the area formed by the overlap of the capillary entrance circle with the same circle shifted upwards by the distance y_m. Figure 7 shows these circles, each of which contains an overlapping area shaded by vertical lines. When an ion enters within this shaded area, it can follow a parabola to its minimum without hitting the lower capillary wall. Since the entrance patch ends at this minimum, the ions travel without further disturbance to the capillary exit as already demonstrated for $x = 0$ (Fig. 7). It is seen that the overlap area strongly decreases with increasing tilt angle.

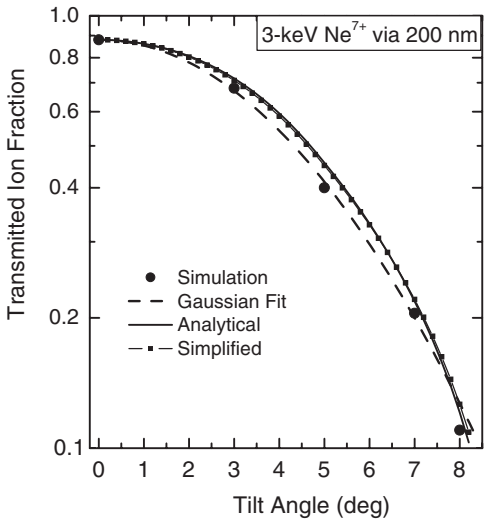

FIG. 8. Transmitted ion fraction as a function of the tilt angle. The thick points are results from the simulations for tilt angles from 0° to 8°. The dashed curve represents fit results using the Gaussian-like function from Eq. (1). The solid line represents results from Eq. (12) together with the analytical expression (13). The line with thin dots is derived from the simplified expression given by Eq. (14).

Let us assume that the loss of the ions within the capillary is small, once it has entered into the overlap area. Then, the transmitted ion fraction is given by the overlap area $\widetilde{\sigma}_t = \sigma_t/\sigma_0$ normalized to the full circular surface $\sigma_0 = \pi d^2/4$,

$$f_t = f_0\,\widetilde{\sigma}_t, \tag{12}$$

where f_0 is the transmitted ion fraction for $\psi = 0$ as in Eq. (1).

The normalized area $\widetilde{\sigma}_t$ can readily be evaluated by splitting it into two equal parts, each of which represents a circular section. These parts can be integrated in closed form, yielding for the overlap area

$$\widetilde{\sigma}_t = 1 - \frac{2}{\pi}\left[\widetilde{y}_m\sqrt{1-\widetilde{y}_m^2} + \arctan\left(\frac{\widetilde{y}_m}{\sqrt{1-\widetilde{y}_m^2}}\right)\right], \tag{13}$$

where $\widetilde{y}_m = y_m/d$ is the relative distance between the two circles. The results from Eq. (12) together with Eq. (13) are given in Fig. 8 as a solid line labeled "Analytical." The analytical curve agrees within a few percent with the thick data points obtained by the simulations. The finding that this curve is somewhat higher than the data points may be attributed to the neglect of the loss of ions entering into the area $\widetilde{\sigma}_t$.

After some trials it was found that the formula (13) can be extremely well approximated by the simple expression

$$\widetilde{\sigma}_t = (1-\widetilde{y}_m)^{\chi} \tag{14}$$

with $\chi = 1.36$. A similar expression with $\chi = 1$ has been derived for ion guiding between parallel plates [36]. The results from Eq. (14) are also shown in Fig. 7 as a solid line with small rectangular dots labeled "Simplified." The agreement between the results of Eqs. (13) and (14) is so good that the differences can barely be seen in the figure.

One may ask why a simpler formula is introduced to replace the original one, which is already analytical and simple enough. The reason for the replacement is that the simpler expression (14) can more easily be used for further developments. The drawback of both analytical expressions (13) and (14) is that the calculated ion fraction f_t may become negative for higher tilt angles ($>10^\circ$). This unphysical feature originates from the various approximations used to evaluate the analytical expressions, such as the assumption of a constant E_y field.

To avoid the negative results one may suppose that the two terms in Eq. (14) are the zero- and first-order contributions of a Taylor-like power expansion in $\widetilde{y}_m$, which can be extended by adding some higher-order terms:

$$\widetilde{\sigma}_t = (1 - \widetilde{y}_m + c_2\widetilde{y}_m^2 - c_3\widetilde{y}_m^3 + \ldots)^{\chi}. \tag{15}$$

With adequate constants c_2 and c_3 one may approximate this series by the exponential function $\widetilde{\sigma}_t \approx \exp(-\widetilde{y}_m)^{\chi} = \exp(-\chi\widetilde{y}_m)$. The second- and higher-order terms play a role only at larger values of ψ. Replacing $\widetilde{y}_m$ by means of Eq. (12), the exponential function can be rewritten as

$$f_t = f_0 \exp\left(-\frac{\sin^2\psi}{\sin^2\psi_d}\right), \tag{16}$$

where the characteristic angle ψ_d is given by

$$\sin\psi_d = \left(\frac{qV_d}{\chi T_p}\right)^{0.5} \tag{17}$$

with $V_d = E_y d$, which is equal to the transverse potential across the capillary diameter d.

Hence, with Eq. (16) the same Gaussian-like function is obtained as in Eq. (1), which is widely used in the literature. Also, the expressions for the characteristic angles ψ_d and ψ_c are similar. With the field of $E_y = 0.04$ V/nm from Table IV, it follows that $\psi_d = 6.7^\circ$, which compares reasonably well with the guiding angle of $\psi_c = 5.6^\circ$ given above. [Nevertheless, Eq. (17) overestimates the simulations, which may again be attributed to the neglect of the ion loss mentioned above.] However, we have to keep in mind that Eq. (17) was derived on the basis of simple approximations, and does not contain a free parameter, whereas Eq. (1) was empirically introduced with the guiding angle as a fit parameter.

Here, it should not be suggested that Eq. (17) be used instead of Eq. (2), since the latter has been proven to successfully reproduce the dependence of the guiding angle on the charge-to-energy ratio q/T_p [7,12]. The value of Eq. (17) lies in its ability to answer a long-standing open question. It is recalled from the discussion in Sec. II that V_c was introduced as an unspecified potential, which was treated as a fit parameter independent of the tilt angle ψ.

The parameter V_c could in principle be identified with the quantity U_e [30] which, however, is not a good choice as it varies with ψ. Rather, with Eq. (17) it now becomes evident that V_c should be identified with a value proportional to V_d. The present numbers suggest that $V_c \approx 2V_d$ would be a good choice. This identification is favorable since the potential V_d is nearly constant due to the fact that E_y is only marginally dependent on the tilt angle ψ.

VI. CONCLUSIONS

Simulations for the guiding of 3-keV Ne^{7+} ions through a nanocapillary are conducted using methods for a nonlinear charge transport previously developed in (I). The calculations are focused on ion-guiding mechanisms for different tilt angles. It is shown that the oscillations of the mean emission angle of the transmitted ions compare well with previous experimental results. Moreover, the tilt-angle dependence of the transmitted ion fraction can be well fitted by a Gaussian-like function. The fit allows for the determination of the guiding angle in good agreement with experimental results used to set up scaling rules for ion guiding. The agreement with the experimental studies provides confidence that the general concepts of the simulations are adequate.

The results of the simulations are taken as a basis to establish an analytical formalism, which describes the characteristic properties of ion guiding. The use of a Gaussian function for the description of the transmitted ion fraction is made plausible. The formalism yields a characteristic angle in closed form which contains the potential V_d. The latter potential is identified with the unspecified potential V_c that governs the guiding angle. This identification is suitable since both potentials are supposed to depend only weakly on the tilt angle. On the other hand, both potentials and, thus, the corresponding guiding angle, are expected to depend on the conductivity of the material, which has indeed been shown in recent experiments [22].

The challenging part of the simulations is the modeling of the charge flow along the capillary surface, which supports the self-organized production of the entrance charge patch. As in (I), it is found that the major effect on the charge patch originates from the transverse charge transport to the opposite capillary wall. This transverse charge transport is expected to compensate the E_y field significantly. Therefore, particular care is required in adequately modeling the transverse charge flow.

The major purpose of the simulations is to reveal unknown mechanisms of the guiding process. Unexpected and controversial results are found from the calculations. Various results simplify the scenario of capillary guiding so that it is possible to derive analytical expressions as noted above. The analytical expressions essentially confirm the unexpected findings from the simulations. The most important results are as follows.

(i) The component E_x is minor at all locations within the capillary.

(ii) The component E_y is nearly constant with respect to the x and y directions and in a certain z range within the capillary entrance region.

(iii) The component E_y changes only marginally with varying tilt angle ψ.

(iv) The component E_y in the z direction is expanded proportionally to $\sin\psi$.

(v) The expansion of E_y is responsible for the increasing deflection of the ions with increasing ψ.

(vi) The component E_y decreases with increasing charge insertion.

The items (i) to (v) refer to equilibrium conditions, whereas item (vi) is concerned with the dynamics of the guiding process. All items allow for various conclusions, which can be summarized as follows.

Item (i) implies that the component E_x may be neglected in the calculations to save computing time. Nevertheless, to be on the safe side, E_x was taken into account in all calculations.

Item (ii) simplifies the analytical treatment of the ion trajectories. The constancy of E_y results in ion movements along parabolic curves.

Item (iii) is definitely counterintuitive. To achieve guiding conditions the ions must be deflected by at least the tilt angle. Thus, one would expect the deflecting field to increase with tilt angle to compensate the y component of the incident energy, which increases with $\sin^2\psi$.

Item (iv) is also counterintuitive. The extension of E_y with tilt angle appears to contradict the length decrease of the charge patch produced by the undeflected ion beam. This contradiction is explained by changes of the charge patch length with ion deposition. In fact, the simulations indicate that for the tilt angle of 3° the charge patch shrinks, whereas for 7° the charge patch is expanded during charge deposition. The analytical functions of the parabolic trajectories show the same phenomenon.

Item (v) can be explained by a combination of (iii) and (iv). The increasing ion deflection with tilt angle is not determined by the (constant) field strength but by the increasing length of the E_y field in z direction.

Item (vi) is relevant for the dynamics of the ion guiding. The decrease of the E_y field with charge insertion is the reason for the oscillation of the emission angle and the steady transmission at equilibrium. At the beginning of the ion deposition the E_y field increases rapidly to a maximum so that the ions are deflected to the opposite capillary wall where they create a transient charge patch. With increasing charge deposition the E_y field decreases until the ions are transmitted directly to the capillary exit. The decrease of the E_y field is still a surprise. It can be associated with the migration of the deposited charges to the other side of the capillary wall which involves a double effect. The migration not only reduces the charge in the entrance patch but also builds up a field opposite to the original E_y field.

The unexpected decrease of the field component E_y with increasing charge insertion is the key for interpreting the self-organization of ion guiding. This phenomenon is not fully understood, as the analysis of the dynamics of the charge patch formation is still incomplete. The present results show that the variation of the repulsive field E_y depends sensitively on the transport of the charges to the opposite side of the entrance patch. This transverse charge transport should be accurately included in models developed to reproduce the decrease of the transverse field component. With the present analytical expression the modeling of the dynamic guiding properties should be facilitated. In any case, the dynamical aspect associated with the self-organization of the ion-guiding phenomenon merits future attention.

ACKNOWLEDGMENTS

I am much indebted to Christoph Lemell, Grigori Pokhil, Yasu Yamazaki, and Bela Sulik for several stimulating and clarifying discussions. Several comments on the manuscript by John Tanis are gratefully acknowledged.

[1] N. Stolterfoht, J. H. Bremer, V. Hoffmann, R. Hellhammer, D. Fink, A. Petrov, and B. Sulik, Phys. Rev. Lett. **88**, 133201 (2002).

[2] N. Stolterfoht, V. Hoffmann, R. Hellhammer, D. Fink, A. Petrov, Z. D. Pešić, and B. Sulik, Nucl. Instrum. Methods Phys. Res. B **203**, 246 (2003).

[3] N. Stolterfoht, R. Hellhammer, Z. D. Pešić, V. Hoffmann, J. Bundesmann, A. Petrov, D. Fink, and B. Sulik, Vacuum **73**, 31 (2004).

[4] Y. Kanai, M. Hoshino, T. Kambara, T. Ikeda, R. Hellhammer, N. Stolterfoht, and Y. Yamazaki, Nucl. Instrum. Methods Phys. Res. B **258**, 155 (2007).

[5] R. Hellhammer, J. Bundesmann, D. Fink, and N. Stolterfoht, Nucl. Instrum. Methods Phys. Res. B **258**, 159 (2007).

[6] N. Stolterfoht, R. Hellhammer, J. Bundesmann, D. Fink, Y. Kanai, M. Hoshino, T. Kambara, T. Ikeda, and Y. Yamazaki, Phys. Rev. A **76**, 022712 (2007).

[7] N. Stolterfoht, R. Hellhammer, J. Bundesmann, and D. Fink, Phys. Rev. A **77**, 032905 (2008).
[8] M. Kreller, G. Zschornak, and U. Kentsch, J. Phys.: Conf. Ser. **163**, 012090 (2009).
[9] N. Stolterfoht, R. Hellhammer, Z. Juhász, B. Sulik, E. Bodewits, H. M. Dang, and R. Hoekstra, Phys. Rev. A **82**, 052902 (2010).
[10] Z. Juhász, B. Sulik, R. Rácz, S. Biri, R. J. Bereczky, K. Tőkési, Á. Köver, J. Pálinkás, and N. Stolterfoht, Phys. Rev. A **82**, 062903 (2010).
[11] D. Li, Y. Wang, Y. Zhao, G. Xiao, D. Zhao, Z. Xu, and F. Li, Nucl. Instrum. Methods Phys. Res. B **267**, 469 (2009).
[12] N. Stolterfoht, R. Hellhammer, Z. Juhász, B. Sulik, V. Bayer, C. Trautmann, E. Bodewits, A. J. de Nijs, H. M. Dang, and R. Hoekstra, Phys. Rev. A **79**, 042902 (2009).
[13] M. B. Sahana, P. Skog, G. Víkor, R. T. RajendraKumar, and R. Schuch, Phys. Rev. A **73**, 040901 (2006).
[14] S. Mátéfi-Tempfli, M. Mátéfi-Tempfli, L. Piraux, Z. Juhász, S. Biri, É. Fekete, I. Iván, F. Gáll, B. Sulik, G. Víkor *et al.*, Nanotechnology **17**, 3915 (2006).
[15] P. Skog, I. L. Soroka, A. Johansson, and R. Schuch, Nucl. Instrum. Methods Phys. Res. B **258**, 145 (2007).
[16] Z. Juhász, B. Sulik, S. Biri, I. Iván, K. Tőkési, É. Fekete, S. Mátéfi-Tempfli, M. Mátéfi-Tempfli, G. Víkor, E. Takács *et al.*, Nucl. Instrum. Methods Phys. Res. B **267**, 321 (2009).
[17] P. Skog, H. Zhang, and R. Schuch, Phys. Rev. Lett. **101**, 223202 (2008).
[18] Y. Kanai, M. Hoshino, T. Kambara, T. Ikeda, R. Hellhammer, N. Stolterfoht, and Y. Yamazaki, Phys. Rev. A **79**, 012711 (2009).
[19] N. Stolterfoht, R. Hellhammer, D. Fink, B. Sulik, Z. Juhász, E. Bodewits, H. M. Dang, and R. Hoekstra, Phys. Rev. A **79**, 022901 (2009).
[20] H. Zhang, P. Skog, and R. Schuch, Phys. Rev. A **82**, 052901 (2010).
[21] B. S. Dassanayake, R. J. Bereczky, S. Das, A. Ayyad, K. Tőkési, and J. A. Tanis, Phys. Rev. A **83**, 012707 (2011).
[22] E. Gruber, G. Kowarik, F. Ladening, J. P. Waclawek, F. Aumayr, R. J. Bereczky, K. Tőkési, P. Gunacker, T. Schweigler, C. Lemell *et al.*, Phys. Rev. A **86**, 062901 (2012).
[23] K. Schiessl, W. Palfinger, C. Lemell, and J. Burgdörfer, Nucl. Instrum. Methods Phys. Res. B **232**, 228 (2005).
[24] K. Schiessl, W. Palfinger, K. Tőkési, H. Nowotny, C. Lemell, and J. Burgdörfer, Phys. Rev. A **72**, 062902 (2005).
[25] K. Schiessl, W. Palfinger, K. Tőkési, H. Nowotny, C. Lemell, and J. Burgdörfer, Nucl. Instrum. Methods Phys. Res. B **258**, 150 (2007).
[26] K. Schiessl, C. Lemell, K. Tőkési, and J. Burgdörfer, J. Phys.: Conf. Ser. **163**, 012081 (2009).
[27] K. Schiessl, K. Tőkési, B. Solleder, C. Lemell, and J. Burgdörfer, Phys. Rev. Lett. **102**, 163201 (2009).
[28] N. Stolterfoht, Phys. Rev. A **87**, 012902 (2013).
[29] J. Frenkel, Phys. Rev. **54**, 647 (1938).
[30] N. Stolterfoht, R. Hellhammer, B. Sulik, Z. Juhász, V. Bayer, C. Trautmann, E. Bodewits, and R. Hoekstra, Phys. Rev. A **83**, 062901 (2011).
[31] N. Stolterfoht, R. Hellhammer, J. Bundesmann, and D. Fink, Radiat. Eff. Defects Solids **162**, 515 (2007).
[32] D. K. Davies, J. Phys. D **5**, 162 (1972).
[33] K. Hayashi, K. Yoshino, and Y. Inuishi, Jpn. J. Appl. Phys **14**, 39 (1975).
[34] Data sheets for PET (Mylar) from DuPont Teijin Films [www.dupontteijinfilms.com].
[35] Data sheets for PC (Lexan) from Sabic Innovative Plastics [www.sabic-ip.com].
[36] G. P. Pokhil, K. A. Vokhmyanina, L. A. Zhilyakov, T. Ikeda, Y. Kanai, Y. Iwai, T. M. Kojima, and Y. Yamazaki, Bulletin. Russ. Acad. Sci.: Phys. **72**, 638 (2008).